



Novel magnetic $\text{CoFe}_2\text{O}_4/\text{Ag}/\text{Ag}_3\text{VO}_4$ composites: Highly efficient visible light photocatalytic and antibacterial activity



Liquan Jing^a, Yuanguo Xu^a, Shuquan Huang^a, Meng Xie^a, Minqiang He^{a,*}, Hui Xu^a, Huaming Li^{a,*}, Qi Zhang^b

^a School of Chemistry and Chemical Engineering, School of Pharmacy, Jiangsu University, Zhenjiang 212013, PR China

^b Hainan Provincial Key Lab of Fine Chemistry, Hainan University, Haikou, Hainan 570228, PR China

ARTICLE INFO

Article history:

Received 10 December 2015

Received in revised form 6 April 2016

Accepted 20 May 2016

Available online 1 June 2016

Keywords:

Magnetic

$\text{CoFe}_2\text{O}_4/\text{Ag}/\text{Ag}_3\text{VO}_4$

Photocatalytic

Antibacterial

ABSTRACT

Visible-light-driven magnetic $\text{CoFe}_2\text{O}_4/\text{Ag}/\text{Ag}_3\text{VO}_4$ photocatalysts with different weight ratios of CoFe_2O_4 were successfully synthesized by a hydrothermal method. The as-prepared samples have been characterized by X-ray diffraction (XRD), infrared (IR), scanning electron microscopy with an energy-dispersive X-ray spectrometer (SEM-EDS), transmission electron microscope (TEM), X-ray photoelectron spectroscopy (XPS), Ultraviolet-visible absorption spectroscopy (UV-vis) and vibrating sample magnetometer (VSM). The photocatalytic experiments indicate that the $\text{CoFe}_2\text{O}_4/\text{Ag}/\text{Ag}_3\text{VO}_4$ composites possess enhanced visible-light-driven photocatalytic activity towards the degradation of methyl orange (MO), tetracycline (TC) and killing Escherichia coli (*E. coli*). Electrochemical impedance spectroscopy (EIS) and photoluminescence (PL) spectra analysis indicate that the introduction of CoFe_2O_4 could efficiently promote the separation efficiency of photogenerated charge carriers in $\text{Ag}/\text{Ag}_3\text{VO}_4$. It is obvious that the composites show better photocatalytic activity than the pure $\text{Ag}/\text{Ag}_3\text{VO}_4$ and CoFe_2O_4 . In particular, the 5% $\text{CoFe}_2\text{O}_4/\text{Ag}/\text{Ag}_3\text{VO}_4$ sample shows the highest photocatalytic activity and the degradation constant of 5% $\text{CoFe}_2\text{O}_4/\text{Ag}/\text{Ag}_3\text{VO}_4$ is as high as 3.4 times to that of $\text{Ag}/\text{Ag}_3\text{VO}_4$. The trapping experiments show that $\bullet\text{O}_2^-$ and h^+ are the major reactive species for the $\text{CoFe}_2\text{O}_4/\text{Ag}/\text{Ag}_3\text{VO}_4$ photocatalytic system. In addition, the as-prepared $\text{CoFe}_2\text{O}_4/\text{Ag}/\text{Ag}_3\text{VO}_4$ composite can be quickly separated from the solution by an extra magnetic field after the photocatalytic reaction. The cyclic test and the XRD patterns before and after cyclic test show that the $\text{CoFe}_2\text{O}_4/\text{Ag}/\text{Ag}_3\text{VO}_4$ hybrid materials have the stable degradation ability and crystal structure during the photodegradation process. Furthermore, it shows highly efficient visible light photocatalytic antibacterial activity. In all, the $\text{CoFe}_2\text{O}_4/\text{Ag}/\text{Ag}_3\text{VO}_4$ photocatalyst, as the magnetic photocatalyst and antibacterial, is promising for the further practical application of photocatalysis in wastewater treatment.

© 2016 Elsevier B.V. All rights reserved.

1. Introduction

Nowadays, environment and energy issues are very serious, which have attracted people's attention. The treatment of various organic pollutants in wastewater is a major aspect of environmental issues. At the same time, bacteria in the sewage should be killed to avoid pathogenic. Recently, semiconductor catalyst has been widely used in the treatment of organic pollutants in wastewater. Among all the semiconductors, TiO_2 has been widely used in the research of photocatalytic degradation of organic pollutants and killing pathogenic pathogens to solve environmental pollu-

tion problems because of their good chemical properties, low cost, stable physical properties and good photocatalytic activity. However, TiO_2 has a large band gap and low quantum efficiency, which restricts its practical application [1,2].

In recent years, a lot of novel Ag-based photocatalytic materials have been used as promisingly efficient photocatalysts and well-known photosensitive materials, such as AgX ($\text{X} = \text{Cl}, \text{Br}, \text{I}$) [3], Ag_2CO_3 [4–6], AgVO_3 [7–9], Ag_3PO_4 [10–12]. Among these Ag-based catalysts, Ag_3VO_4 was reported to possess photocatalytic activity, which is mainly due to the narrow band gap and the special band structure [13]. However, due to high recombination of photogenerated electron-hole pairs, the photocatalytic property of pure Ag_3VO_4 was restricted [14,15]. To advance this promising photocatalytic material, researchers have coupled Ag_3VO_4 with other semiconductors to increase the separation efficiency of

* Corresponding authors.

E-mail addresses: jbmwgk@126.com (M. He), lh@ujs.edu.cn (H. Li).

photogenerated electron-hole pairs, thus to improve the photocatalytic performance. For example, $\text{ZnO}/\text{Ag}_3\text{VO}_4$ [13], $\text{Co}_3\text{O}_4/\text{Ag}_3\text{VO}_4$ [14], $\text{TiO}_2/\text{Ag}_3\text{VO}_4$ [16], $\text{NiO}/\text{Ag}_3\text{VO}_4$ [17], $\text{CoTiO}_3/\text{Ag}_3\text{VO}_4$ [18], $\text{NiTiO}_3/\text{Ag}_3\text{VO}_4$ [19], $\text{MgFe}_2\text{O}_4/\text{Ag}_3\text{VO}_4$ [20], $\text{ZnFe}_2\text{O}_4/\text{Ag}_3\text{VO}_4$ [21], $\text{BiOI}/\text{Ag}_3\text{VO}_4$ [22], $\text{g-C}_3\text{N}_4/\text{Ag}_3\text{VO}_4$ [23] and $\text{Ag}_3\text{VO}_4/\text{AgBr}/\text{Ag}$ [24]. However, these Ag_3VO_4 -based photocatalysts face difficulty of separation after photocatalytic reactions, which limits their application in practical fields. To solve this problem, magnetic nanoparticles as photocatalyst carrier have been proposed to obtain the efficient recyclable Ag-based materials for water treatment. There are many catalysts combined with magnetic materials to improve the recycle ability, such as $\text{Fe}_3\text{O}_4@\text{LDH}@\text{Ag}/\text{Ag}_3\text{PO}_4$ [25], $\gamma\text{-Fe}_2\text{O}_3@\text{SiO}_2@\text{AgBr}:\text{Ag}$ [26], $\text{Ag}/\text{AgCl}/\text{CoFe}_2\text{O}_4$ [27], $\text{Ag}/\text{NiFe}_2\text{O}_4$ [28], carbon microspheres (CMSs)@ $\text{ZnFe}_2\text{O}_4/\text{Ag}_3\text{PO}_4$ [29]. Among these magnetic materials, cobalt ferrite (CoFe_2O_4) has the remarkable chemical stability, large magnetic anisotropy and mechanical hardness [30]. Therefore, CoFe_2O_4 has been widely used for photocatalytic degradation of organic pollutants or magnetic separation [31]. Several previous studies have been reported. For example, Singh et al. [32] synthesized CdS nanorods decorated with CoFe_2O_4 nanoparticles by using a facile soft chemical method. The composites exhibited enhanced visible light driven photocatalytic activity for the degradation of methylene blue (MB), which were also able to be magnetic separated. Wetchakun et al. [33] fabricated $\text{CoFe}_2\text{O}_4/\text{CeO}_2$ nanocomposite materials by coupling a precipitation method with hydrothermal method, which were used as a magnetic photocatalyst for degrading organic pollutant. In addition, other composite materials have also been reported, such as $\text{TiO}_2/\text{CoFe}_2\text{O}_4$ [34], $\text{CoFe}_2\text{O}_4/\text{ZnO}$ [35], $\text{CoFe}_2\text{O}_4/\text{graphene}$ [36]. Excitingly, all of the catalysts combined with CoFe_2O_4 show varying degree of enhanced photocatalytic activity.

According to the above analysis, $\text{Ag}/\text{Ag}_3\text{VO}_4$ modified with CoFe_2O_4 may improve the photocatalytic activity and possess magnetic separation ability. In this work, the new magnetic photocatalyst $\text{CoFe}_2\text{O}_4/\text{Ag}/\text{Ag}_3\text{VO}_4$ hybrid materials were synthesized by a facile hydrothermal method. As expected, the as-prepared hybrid materials exhibit enhanced photocatalytic activities for the degradation of methyl orange (MO), tetracycline (TC). Besides, the hybrid materials exhibit good antibacterial activity against *Escherichia coli* (*E. coli*) under visible light irradiation. The cyclic test shows that the $\text{CoFe}_2\text{O}_4/\text{Ag}/\text{Ag}_3\text{VO}_4$ hybrid materials have stable degradation ability and the XRD patterns before and after cyclic test indicates that the composites possess the stable crystal structures during the photodegradation process. The trapping experiments show that $\bullet\text{O}_2^-$ and h^+ are the major reactive species for the $\text{CoFe}_2\text{O}_4/\text{Ag}/\text{Ag}_3\text{VO}_4$ photocatalytic system. Thus, this research shows that $\text{CoFe}_2\text{O}_4/\text{Ag}/\text{Ag}_3\text{VO}_4$ composites possess excellent photocatalytic degradation performance, antibacterial properties and magnetic recovery performance.

2. Experiment

2.1. Materials

All chemicals were analytical reagent grade and used without additional purification or treatment.

2.2. Synthesis of CoFe_2O_4 nanoparticles

The synthesis of cobalt ferrite nanoparticles refers to our previous work [27]. 10 mmol $\text{Fe}(\text{NO}_3)_3 \cdot 9\text{H}_2\text{O}$ and 5 mmol $\text{Co}(\text{NO}_3)_2 \cdot 6\text{H}_2\text{O}$ were dissolved in 100 mL distilled water. The abovementioned solution was referred as solution A. Meanwhile, 15 mmol $\text{C}_6\text{H}_8\text{O}_7 \cdot \text{H}_2\text{O}$ was added into 100 mL distilled water (referred as solution B). Then, the solution A was added dropwise

into solution B with stirring and the temperature was maintained at 60 °C. After stirring for 1 h, the mixture solution was placed in an oven and dried at 90 °C for about 24 h. The obtained solid composite was then calcined at 300 °C and allowed to stand for 2 h.

2.3. Synthesis of $\text{CoFe}_2\text{O}_4/\text{Ag}/\text{Ag}_3\text{VO}_4$

$\text{CoFe}_2\text{O}_4/\text{Ag}/\text{Ag}_3\text{VO}_4$ was obtained by the hydrothermal method. A certain quality of CoFe_2O_4 nanoparticles were ultrasonically dispersed into 40 mL deionized water for 10 min. 0.24 g of AgNO_3 was added into the above solution followed by stirring by the mechanical agitation with the polytetrafluoroethylene stirring rod in the ice water bath for 30 min. At the same time, 0.1884 g of $\text{Na}_3\text{VO}_4 \cdot 12\text{H}_2\text{O}$ was dissolved in another 40 mL deionized water and stirred in the ice water bath for 30 min. Subsequently, the solution with Na_3VO_4 was totally injected into the above mixture solution. Then the mixture was keeping stirring for further 30 min in the ice water bath. At last, 20 mL of the suspension was transferred to 25 mL Teflon-lined autoclave and heated at 140 °C for 6 h. After that the autoclave was naturally cooled down to room temperature, the resultant product was collected by centrifugation and washed three times by deionized water and ethanol. The products were dried overnight at 60 °C. According to the weight ratio of CoFe_2O_4 to AgNO_3 ($\text{CoFe}_2\text{O}_4:\text{AgNO}_3 = 1\%, 5\%, 10\%, 20\%$, respectively), the obtained products were noted as 1% $\text{CoFe}_2\text{O}_4/\text{Ag}/\text{Ag}_3\text{VO}_4$, 5% $\text{CoFe}_2\text{O}_4/\text{Ag}/\text{Ag}_3\text{VO}_4$, 10% $\text{CoFe}_2\text{O}_4/\text{Ag}/\text{Ag}_3\text{VO}_4$, 20% $\text{CoFe}_2\text{O}_4/\text{Ag}/\text{Ag}_3\text{VO}_4$, respectively. $\text{Ag}/\text{Ag}_3\text{VO}_4$ was obtained without adding CoFe_2O_4 in the synthesis process.

2.4. Characterization

The X-ray diffraction (XRD) patterns of the crystal phase was carried out at room temperature using a Bruker D8 diffractometer with high-intensity $\text{Cu-K}\alpha$ in the 2θ range of 10–80°. The IR spectrum of all the catalysts (KBr pellets) were recorded on the Nicolet Model Nexus 470 IR equipment. The microcrystalline structure and surface characteristics of the samples were obtained by using scanning electron microscope (JEOL-JEM-2010, accelerating voltage 200 kV), which was equipped with an energy-dispersive X-ray spectroscope (acceleration voltage of 10 kV). X-ray photoelectron spectroscopy (XPS) was measured on a PHI5300 with a monochromatic $\text{Mg K}\alpha$ source to explore the elements of the surface. The UV-vis absorption spectroscopy (in the diffuse reflectance spectroscopy model) of the samples were carried out on a Shimadzu UV-2450 spectrophotometer (Shimadzu Corporation, Japan) using BaSO_4 as the reference. The magnetic properties of the CoFe_2O_4 and $\text{CoFe}_2\text{O}_4/\text{Ag}/\text{Ag}_3\text{VO}_4$ composites were measured in a vibrating sample magnetometer (Quantum Design Corporation, USA) with a maximum applied field of $\pm 2\text{ T}$. Electrochemistry analysis was performed on an electrochemical workstation (CHI 660B, Chenhua Instrument Company, Shanghai, China). The photoluminescence (PL) spectra of the photocatalysts were obtained by Varian Cary Eclipse spectrometer with an excitation wavelength of 360 nm.

2.5. Photocatalytic tests

The activity of $\text{CoFe}_2\text{O}_4/\text{Ag}/\text{Ag}_3\text{VO}_4$ was tested by the degradation of Methyl orange (MO) and Tetracycline (TC) under visible light irradiation. In this experiment, 70 mg of samples and 70 mL of aqueous solution of MO were added into the light reaction bottle. For Tetracycline (TC), 50 mg catalysts were dispersed into 100 mL of their aqueous solution, respectively. The suspension was stirred in the dark reaction for 30 min to achieve adsorption equilibrium between catalyst and pollutants. After a certain period of time, the

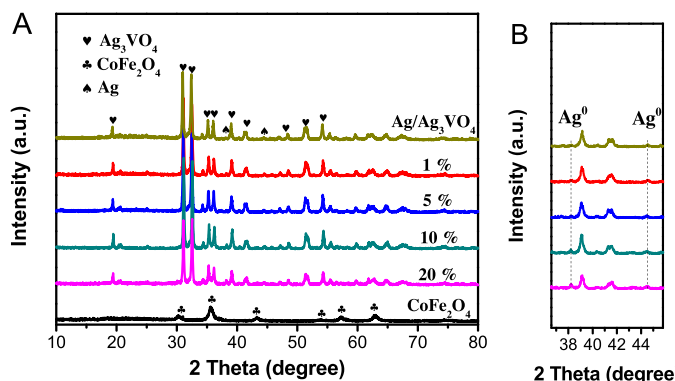


Fig. 1. (A) XRD patterns of $\text{Ag}/\text{Ag}_3\text{VO}_4$, 1% $\text{CoFe}_2\text{O}_4/\text{Ag}/\text{Ag}_3\text{VO}_4$, 5% $\text{CoFe}_2\text{O}_4/\text{Ag}/\text{Ag}_3\text{VO}_4$, 10% $\text{CoFe}_2\text{O}_4/\text{Ag}/\text{Ag}_3\text{VO}_4$, 20% $\text{CoFe}_2\text{O}_4/\text{Ag}/\text{Ag}_3\text{VO}_4$ and CoFe_2O_4 ; (B) Narrow-scan diffraction patterns from 36.6° to 45.8° .

suspension of the 4 mL was taken out and the catalyst was removed to measure the absorbance of the solution by UV-vis spectrophotometer (UV-2450, Shimadzu).

2.6. Antibacterial activities

All the glassware and the culture medium solution were sterilized by autoclaving at 121°C for 20 min. And all the experiments were processed under sterile conditions.

The antibacterial activities of $\text{CoFe}_2\text{O}_4/\text{Ag}/\text{Ag}_3\text{VO}_4$ composites were evaluated via the inactivation of *Escherichia coli* (*E. coli*) bacteria. The zone of inhibition test was carried out to identify the antibacterial activities in the dark. First, 20 μL of the prepared *Escherichia coli* (*E. coli*) bacteria suspension was dispersed on a nutrient agar medium. Then, powder photocatalysts were dispersed on the nutrient agar medium. Then the plates were incubated at 37°C for 24 h in the dark.

The photocatalytic antibacterial experiments were performed by using the following typical method. First, 1 mg of the as-prepared sample was suspended in 20 mL culture medium solutions. Then, a certain volume of the prepared *Escherichia coli* (*E. coli*) bacterial suspension was transferred into $1/(1 \times 10^3)$ concentration. Then the mixture was magnetically stirred in the dark for 30 min, 20 μL of the solution was sampled at the time intervals of 0 min, 4 min, 8 min and 12 min. Each solution was dispersed on the nutrient agar medium and incubated at 37°C for 24 h in dark.

3. Results and discussion

3.1. XRD analysis

Fig. 1A shows the XRD patterns of as-synthesized CoFe_2O_4 , $\text{Ag}/\text{Ag}_3\text{VO}_4$ and different proportions of $\text{CoFe}_2\text{O}_4/\text{Ag}/\text{Ag}_3\text{VO}_4$ magnetic photocatalyst. As shown in **Fig. 1A**, the diffraction peaks at 19.32° , 30.96° , 32.42° , 35.16° , 36.02° , 39.02° , 41.38° , 48.36° , 51.48° and 54.10° are attributed to (011), (-121), (121), (301), (202), (022), (400), (-322), (132) and (331) planes of Ag_3VO_4 (JCPDS No. 43-0542) [22]. The weak peaks appear at $2\theta = 38.12^\circ$ and 44.30° , which can be ascribed to metal Ag^0 (JCPDS No. 04-0783) [37–40]. The pure CoFe_2O_4 sample shows the diffraction peaks at 30.06° , 35.26° , 43.02° , 53.44° , 56.94° and 62.66° , which can be indexed to the CoFe_2O_4 (220), (311), (222), (400), (422) and (511) planes, respectively (JCPDS No. 22-1086) [27]. For the composites, all the characteristic peaks belonging to Ag_3VO_4 did not shift in the $\text{CoFe}_2\text{O}_4/\text{Ag}/\text{Ag}_3\text{VO}_4$ composites, which indicated that the introduction of CoFe_2O_4 did not change the crystal phase structure of Ag_3VO_4 . In addition, diffraction peaks of the Ag^0 at $2\theta = 38.12^\circ$

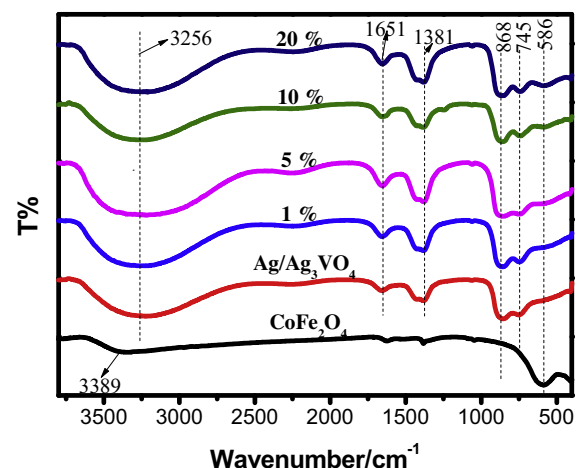


Fig. 2. IR spectra of the samples: CoFe_2O_4 , $\text{Ag}/\text{Ag}_3\text{VO}_4$, 1% $\text{CoFe}_2\text{O}_4/\text{Ag}/\text{Ag}_3\text{VO}_4$, 5% $\text{CoFe}_2\text{O}_4/\text{Ag}/\text{Ag}_3\text{VO}_4$, 10% $\text{CoFe}_2\text{O}_4/\text{Ag}/\text{Ag}_3\text{VO}_4$ and 20% $\text{CoFe}_2\text{O}_4/\text{Ag}/\text{Ag}_3\text{VO}_4$.

(**Fig. 1B**) are discovered in all $\text{CoFe}_2\text{O}_4/\text{Ag}/\text{Ag}_3\text{VO}_4$ composites. At the same time, the diffraction peaks of CoFe_2O_4 were not observed, which may be due to high dispersion and its diffraction peaks being covered [41]. Therefore, the existence of CoFe_2O_4 will be analyzed by IR, SEM-EDS and XPS.

3.2. IR analysis

Fig. 2 shows the IR spectra of CoFe_2O_4 , $\text{Ag}/\text{Ag}_3\text{VO}_4$ and $\text{CoFe}_2\text{O}_4/\text{Ag}/\text{Ag}_3\text{VO}_4$ composites. For the samples, the broad absorption bands at 3389 cm^{-1} or 3256 cm^{-1} are related to the O–H stretching vibration of adsorbed water molecules on the surface of samples [13,22]. For the CoFe_2O_4 nanostructures, similar papers indicated that the 500 – 600 cm^{-1} is due to the intrinsic stretching vibrations of metal–oxygen ions (Fe^{3+} – O^{2-}) at tetrahedral sites in spinel structure, hence the peak at 586 cm^{-1} is attributed to the Fe–O stretching vibration mode [42–45]. The peaks at 745 and 868 cm^{-1} for pure Ag_3VO_4 are assigned to the stretching vibration of Ag–V and V–O bonds, respectively [13,22,46]. As for $\text{CoFe}_2\text{O}_4/\text{Ag}/\text{Ag}_3\text{VO}_4$ composites, the similar absorption bands could also be observed. When the content of CoFe_2O_4 is greater than 5%, the absorption band of CoFe_2O_4 becomes more and more obvious (which indicates the presence of CoFe_2O_4). It can be seen that the absorption bands of $\text{Ag}/\text{Ag}_3\text{VO}_4$ and CoFe_2O_4 do not shift. The above results indicate that the structure of $\text{Ag}/\text{Ag}_3\text{VO}_4$ does not change with the introduction of CoFe_2O_4 , which is in good accordance with the XRD analysis.

3.3. SEM-EDS and TEM analysis

The morphology of the as-prepared $\text{Ag}/\text{Ag}_3\text{VO}_4$ particles and $\text{CoFe}_2\text{O}_4/\text{Ag}/\text{Ag}_3\text{VO}_4$ compound materials were examined by SEM. **Fig. 3A** shows that the large irregular particles with diameters of ca. 0.5 – $1\text{ }\mu\text{m}$ are $\text{Ag}/\text{Ag}_3\text{VO}_4$ particles. These particles have a relatively smooth surface and a serious phenomenon of agglomeration. It can be seen that the morphology image of pure CoFe_2O_4 (**Fig. 3B**) is granular. **Fig. 3C** is SEM image of 1% $\text{CoFe}_2\text{O}_4/\text{Ag}/\text{Ag}_3\text{VO}_4$ composites, it can be seen that the introduction of CoFe_2O_4 changes the shape of $\text{Ag}/\text{Ag}_3\text{VO}_4$ particles. However, the surface of $\text{Ag}/\text{Ag}_3\text{VO}_4$ is different from the surface of the pure $\text{Ag}/\text{Ag}_3\text{VO}_4$, a small amount of particles are on the surface of Ag_3VO_4 . **Fig. 3D** shows the morphology image of 5% $\text{CoFe}_2\text{O}_4/\text{Ag}/\text{Ag}_3\text{VO}_4$, it can be seen more particles attached to the surface of $\text{Ag}/\text{Ag}_3\text{VO}_4$ and the surface of $\text{Ag}/\text{Ag}_3\text{VO}_4$ become rough. Similarly, the SEM images of 10% $\text{CoFe}_2\text{O}_4/\text{Ag}/\text{Ag}_3\text{VO}_4$ and 20% $\text{CoFe}_2\text{O}_4/\text{Ag}/\text{Ag}_3\text{VO}_4$ are shown

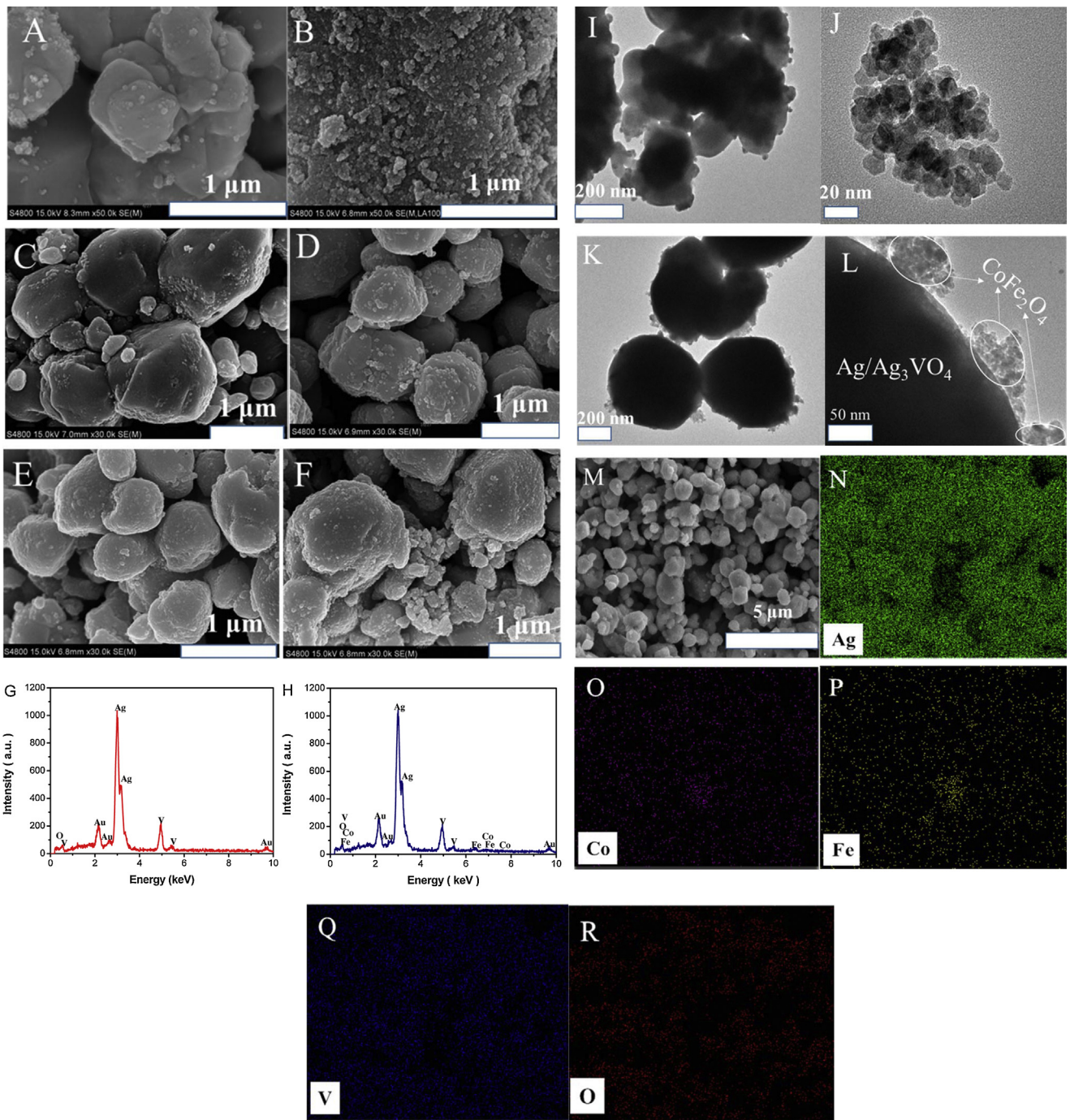


Fig. 3. SEM images of as-prepared samples: (A) $\text{Ag}/\text{Ag}_3\text{VO}_4$, (B) CoFe_2O_4 ; (C) 1% $\text{CoFe}_2\text{O}_4/\text{Ag}/\text{Ag}_3\text{VO}_4$, (D) 5% $\text{CoFe}_2\text{O}_4/\text{Ag}/\text{Ag}_3\text{VO}_4$, (E) 10% $\text{CoFe}_2\text{O}_4/\text{Ag}/\text{Ag}_3\text{VO}_4$, (F) 20% $\text{CoFe}_2\text{O}_4/\text{Ag}/\text{Ag}_3\text{VO}_4$; EDS of (G) $\text{Ag}/\text{Ag}_3\text{VO}_4$ and (H) 5% $\text{CoFe}_2\text{O}_4/\text{Ag}/\text{Ag}_3\text{VO}_4$; TEM images of (I) $\text{Ag}/\text{Ag}_3\text{VO}_4$, (J) CoFe_2O_4 , (K) and (L) 5% $\text{CoFe}_2\text{O}_4/\text{Ag}/\text{Ag}_3\text{VO}_4$; (M) SEM images of 5% $\text{CoFe}_2\text{O}_4/\text{Ag}/\text{Ag}_3\text{VO}_4$ and the corresponding elemental mappings of (N) Ag, (O) Co, (P) Fe, (Q) V, and (R) O elements.

in Fig. 3E and 3F, respectively. Specifically, the surface becomes rougher. It can be seen that the surface structure of $\text{Ag}/\text{Ag}_3\text{VO}_4$ varies with the increase of CoFe_2O_4 content. In addition, when the content of CoFe_2O_4 at a high level ($\geq 10\%$), it can be noticed that $\text{Ag}/\text{Ag}_3\text{VO}_4$ was wrapped. This may decrease the photocatalytic activity of $\text{CoFe}_2\text{O}_4/\text{Ag}/\text{Ag}_3\text{VO}_4$ composites. EDS of the pure $\text{Ag}/\text{Ag}_3\text{VO}_4$ and 5% $\text{CoFe}_2\text{O}_4/\text{Ag}/\text{Ag}_3\text{VO}_4$ are shown in Fig. 3G and H, respectively. Ag, V and O were found in the spectra of $\text{Ag}/\text{Ag}_3\text{VO}_4$, while Ag, V, O, Co and Fe were directly observed in the 5% $\text{CoFe}_2\text{O}_4/\text{Ag}/\text{Ag}_3\text{VO}_4$ composites. The result indicates that the small particles on the surface of $\text{Ag}/\text{Ag}_3\text{VO}_4$ are CoFe_2O_4 nanoparticles.

In order to provide solid evidence that CoFe_2O_4 nanoparticles were successfully combined with $\text{Ag}/\text{Ag}_3\text{VO}_4$, the TEM images are investigated in Fig. 3I–L. Fig. 3I shows the TEM image of pure $\text{Ag}/\text{Ag}_3\text{VO}_4$, these nanoparticles are aggregated. As we can see, the surface of $\text{Ag}/\text{Ag}_3\text{VO}_4$ particles is relatively smooth with small amount nanoparticles. Fig. 3J displays the TEM images of pure CoFe_2O_4 , the size of CoFe_2O_4 nanoparticles are around 20 nm and they are easy to aggregate. As shown in Fig. 3K and L, the TEM images of the $\text{CoFe}_2\text{O}_4/\text{Ag}/\text{Ag}_3\text{VO}_4$ composites clearly display two different shapes. With the addition of CoFe_2O_4 , it is easy to observe that the irregular spherical $\text{Ag}/\text{Ag}_3\text{VO}_4$ particles are

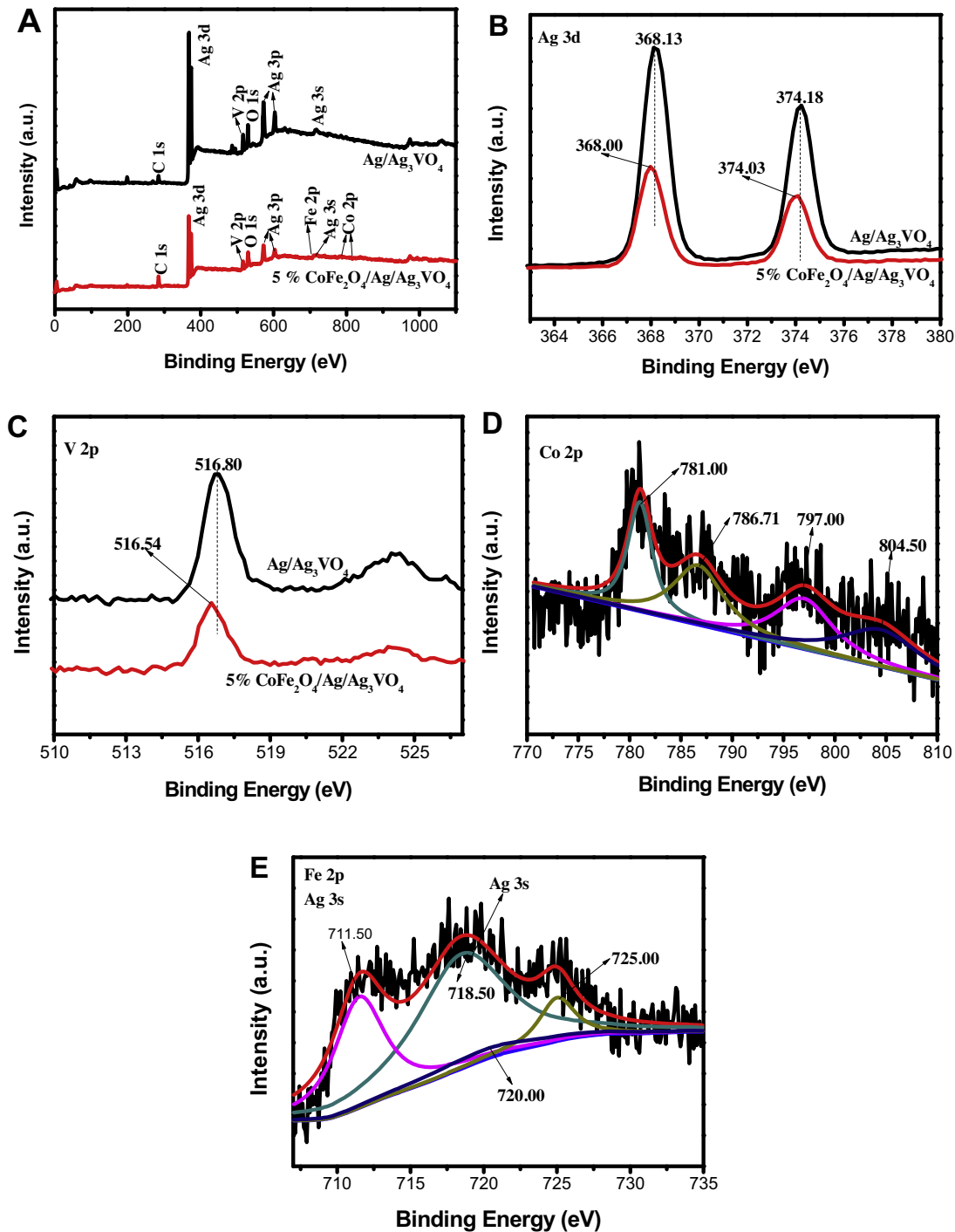


Fig. 4. XPS spectra of $\text{Ag}/\text{Ag}_3\text{VO}_4$ and 5% $\text{CoFe}_2\text{O}_4/\text{Ag}/\text{Ag}_3\text{VO}_4$ composites: (A) the survey scans; (B) Ag 3d; (C) V 2p; (D) Co 2p and (E) Fe 2p of 5% $\text{CoFe}_2\text{O}_4/\text{Ag}/\text{Ag}_3\text{VO}_4$ composites.

loaded by the small agglomerate nanoparticles on the surface (the larger particles are $\text{Ag}/\text{Ag}_3\text{VO}_4$ and the agglomerate nanoparticles are CoFe_2O_4). The formation of $\text{CoFe}_2\text{O}_4/\text{Ag}/\text{Ag}_3\text{VO}_4$ microstructure can fully use the outer surfaces of $\text{Ag}/\text{Ag}_3\text{VO}_4$ and interfaces between $\text{Ag}/\text{Ag}_3\text{VO}_4$ and CoFe_2O_4 , which may improve the separation efficiency of charge carriers and photocatalytic activity of the composite. Moreover, to reveal the distribution of CoFe_2O_4 in the 5% $\text{CoFe}_2\text{O}_4/\text{Ag}/\text{Ag}_3\text{VO}_4$ composite, elemental mapping is performed. As presented in Fig. 3M and N–R, the SEM and corresponding mapping distribution show the existence of Ag, Co, Fe, V and O. Besides, the mapping clearly revealed that both Co and Fe

elements are highly dispersed among the composites, which confirms that CoFe_2O_4 was distributed uniformly in the composites. In order to further analyze the distribution of CoFe_2O_4 on the surface of Ag_3VO_4 single particle, the EDS-mapping of Ag_3VO_4 single particle was measured and showed in Fig. S1. It can be seen that the CoFe_2O_4 highly dispersed on the surface of Ag_3VO_4 single particle. However, this result does not distinguish between Ag and CoFe_2O_4 on the surface of Ag_3VO_4 . Therefore, in order to distinguish between Ag and CoFe_2O_4 on the surface of Ag_3VO_4 , HRTEM image of 5% $\text{CoFe}_2\text{O}_4/\text{Ag}/\text{Ag}_3\text{VO}_4$ composites is shown in Fig. S2. It can be seen that the lattice fringes with spacing of 0.215, 0.296 and

0.206 nm can be indexed to the (400) planes of Ag_3VO_4 , the (220) planes of CoFe_2O_4 , and the (200) planes of Ag, respectively, revealing that the small particles on the surface of Ag_3VO_4 were Ag and CoFe_2O_4 nanoparticles. In summary, the above results confirm the presence of Ag_3VO_4 , CoFe_2O_4 and Ag in the composites.

3.4. XPS analysis

To investigate the elemental compositions and chemical states of the as-prepared samples, XPS measurement was carried out. Fig. 4A shows the survey scan spectra of $\text{Ag}/\text{Ag}_3\text{VO}_4$ and 5% $\text{CoFe}_2\text{O}_4/\text{Ag}/\text{Ag}_3\text{VO}_4$ composites. The obvious peaks of C, Ag, V, Co, Fe can be clearly observed in the composites. As shown in Fig. 4B, A typical Ag 3d XPS spectrum of the samples exhibited two predominant characteristic peaks at 368.13 and 374.18 eV, which belong to Ag 3d_{5/2} and Ag 3d_{3/2}, respectively [47]. When CoFe_2O_4 was introduced, the two peaks shifted to 368.00 and 374.03 eV, respectively. Moreover, the binding energy value of V 2p_{3/2} (Fig. 4C) was observed to be 516.80 eV [23]. The peaks of V 2p_{3/2} for 5% $\text{CoFe}_2\text{O}_4/\text{Ag}/\text{Ag}_3\text{VO}_4$ composites shifted to 516.54 eV. In all, the shifts in Ag 3d and V 2p peaks indicate that the chemical environment in the $\text{CoFe}_2\text{O}_4/\text{Ag}/\text{Ag}_3\text{VO}_4$ composites have changed after the introduction of CoFe_2O_4 and confirm that a strong interaction between CoFe_2O_4 and $\text{Ag}/\text{Ag}_3\text{VO}_4$. [48,49] Meanwhile, it can be seen that the peaks of Ag 3d and V 2p in the $\text{CoFe}_2\text{O}_4/\text{Ag}/\text{Ag}_3\text{VO}_4$ composites are lower than the peaks in $\text{Ag}/\text{Ag}_3\text{VO}_4$, which indicates that CoFe_2O_4 affects the chemical environment on the surface of $\text{Ag}/\text{Ag}_3\text{VO}_4$. The high-resolution XPS spectra of 5% $\text{CoFe}_2\text{O}_4/\text{Ag}/\text{Ag}_3\text{VO}_4$ composites in Fig. 4D showed four peaks, which can be attributed to Co 2p [50]. The peaks centered at 781.00 eV (with a satellite peak at 786.71 eV) and at 797.00 eV (with a satellite peak at 804.50 eV) correspond to Co2p_{3/2} and Co2p_{1/2}, respectively. These four peaks are the characteristic peaks of Co^{2+} [51]. As shown in Fig. 4E, the peaks centered at 711.50 and 725.0 eV correspond to Fe2p_{3/2} and Fe2p_{1/2}, respectively. Besides, the peaks at 720.0 eV belong to the Fe^{3+} satellite, which indicates that the valence state of Fe in the complexes is Fe^{3+} [50,51]. The peaks of Co 2p and Fe 2p indicate that CoFe_2O_4 is present in the complexes, which is consistent with the results of IR spectra. In addition, the peak of Ag 3s was observed in Fig. 4E, which is consistent with the previous reports [52–54]. Based on the above analysis, it can be inferred that the interaction force between CoFe_2O_4 and $\text{Ag}/\text{Ag}_3\text{VO}_4$ existed and the $\text{CoFe}_2\text{O}_4/\text{Ag}/\text{Ag}_3\text{VO}_4$ has been successfully synthesized.

3.5. UV-vis analysis

UV-vis absorption spectra were measured to study the optical property of the as-prepared samples. As shown in Fig. 5A, CoFe_2O_4 has remarkable absorption in whole range of the visible light, which may be due to its black color. $\text{Ag}/\text{Ag}_3\text{VO}_4$ has a strong absorption peak at 470 nm, and its absorption edge is around 620 nm, which corresponds to previous reports and suggests the presence of metallic Ag [55]. Compared to the $\text{Ag}/\text{Ag}_3\text{VO}_4$ sample, the hybrid materials showed enhanced spectral response in the visible region after the introduction of CoFe_2O_4 . This may be due to the gradual deepening color of the composites with the increase of the CoFe_2O_4 content. This phenomenon indicates that the composite can absorb more energy, which may be beneficial for the photocatalytic activity. The band gap of the samples can be estimated according to the following equation:

$$\alpha h\nu = c(h\nu - E_g)^n$$

Where α , $h\nu$, c and E_g is the absorption coefficient, the energy of the incident photon, a constant ($c = 1$) and the band gap, respectively

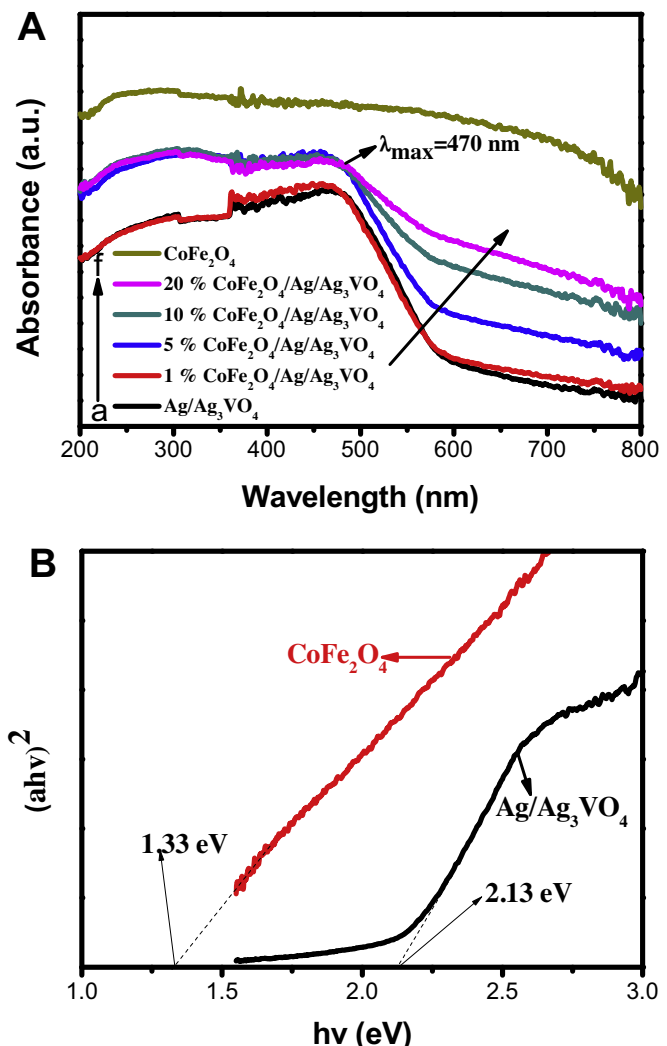


Fig. 5. (A) UV-vis absorption spectra of (a) $\text{Ag}/\text{Ag}_3\text{VO}_4$, (b) 1% $\text{CoFe}_2\text{O}_4/\text{Ag}/\text{Ag}_3\text{VO}_4$, (c) 5% $\text{CoFe}_2\text{O}_4/\text{Ag}/\text{Ag}_3\text{VO}_4$, (d) 10% $\text{CoFe}_2\text{O}_4/\text{Ag}/\text{Ag}_3\text{VO}_4$, (e) 20% $\text{CoFe}_2\text{O}_4/\text{Ag}/\text{Ag}_3\text{VO}_4$ and (f) CoFe_2O_4 . (B) Plots of $(\alpha h\nu)^2$ versus $h\nu$ for $\text{Ag}/\text{Ag}_3\text{VO}_4$ and CoFe_2O_4 .

[52]. Moreover, the value of n describes the type of the transition in a semiconductor. The estimated value of the band gap energies (E_g) can be got by extrapolation of the linear part of the curves obtained by plotting $(\alpha h\nu)^2$ versus $h\nu$. As can be seen, the estimated E_g value of CoFe_2O_4 and $\text{Ag}/\text{Ag}_3\text{VO}_4$ is shown in Fig. 5B. The band gap of CoFe_2O_4 and $\text{Ag}/\text{Ag}_3\text{VO}_4$ were estimated to 1.33 and 2.13 eV, respectively. The results are corresponding to the previous literature reports [30,42,56].

3.6. Magnetic performances

The magnetic property of composites is significant for a recyclable photocatalyst. The magnetic property of CoFe_2O_4 and 5% $\text{CoFe}_2\text{O}_4/\text{Ag}/\text{Ag}_3\text{VO}_4$ was measured using a vibrating sample magnetometer. As shown in Fig. 6, since the complex contains only 5% CoFe_2O_4 , the M_s value for the composite is much smaller than that of pure CoFe_2O_4 , which is due to the presence of the non-magnetic $\text{Ag}/\text{Ag}_3\text{VO}_4$. The detected magnetic saturation (M_s) values of CoFe_2O_4 and 5% $\text{CoFe}_2\text{O}_4/\text{Ag}/\text{Ag}_3\text{VO}_4$ are 29.97 emu g⁻¹ and 1.77 emu g⁻¹, respectively. Obviously, Fig. 6 shows digital photographs that 5% $\text{CoFe}_2\text{O}_4/\text{Ag}/\text{Ag}_3\text{VO}_4$ composites are be separated by an external magnet. The composite can be effectively separated within 1 min. The results indicate that $\text{CoFe}_2\text{O}_4/\text{Ag}/\text{Ag}_3\text{VO}_4$ com-

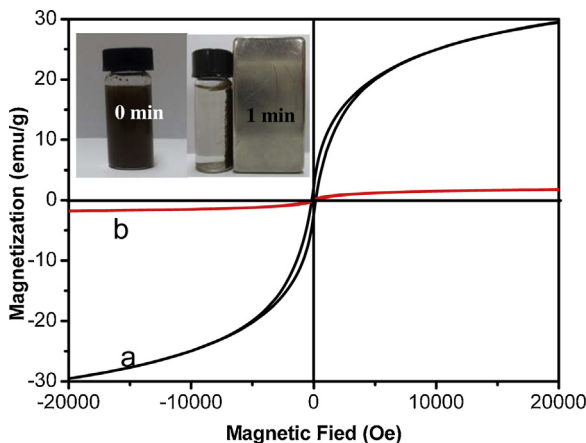


Fig. 6. Field-dependent magnetization curves of CoFe_2O_4 and 5% $\text{CoFe}_2\text{O}_4/\text{Ag}/\text{Ag}_3\text{VO}_4$. The inset photos of 5% $\text{CoFe}_2\text{O}_4/\text{Ag}/\text{Ag}_3\text{VO}_4$ before and after magnetic separation.

posites have an amazing magnetic separation property and can be a promising magnetic photocatalyst material.

3.7. Photocatalytic activity

Fig. 7A shows the photocatalytic activity of $\text{CoFe}_2\text{O}_4/\text{Ag}/\text{Ag}_3\text{VO}_4$ composites with different contents of CoFe_2O_4 under visible light irradiation. The adsorption analysis of the hybrids in the dark for the MO has been shown in Fig. S3. The adsorption–desorption balance have been achieved between the catalyst and dye for 30 min absorption process. It can be seen that 2.7%, 3.9%, 6.6%, 5.5% and 5.3% of MO were respectively adsorbed by $\text{CoFe}_2\text{O}_4/\text{Ag}/\text{Ag}_3\text{VO}_4$ composites with 0%, 1%, 5%, 10% and 20% CoFe_2O_4 within 30 min, which should be attributed to their different adsorption capacity. From Fig. 7A, it can be seen that the photolysis of MO can be negligible in the absence of the catalyst, indicating that the MO is stable under visible light irradiation. CoFe_2O_4 has little photocatalytic degradation ability for MO under visible light irradiation. Meanwhile, for $\text{Ag}/\text{Ag}_3\text{VO}_4$ as the photocatalyst, it can decompose about 51.17% of MO at 16 min. The photocatalytic activity of the $\text{CoFe}_2\text{O}_4/\text{Ag}/\text{Ag}_3\text{VO}_4$ sample increases with the increasing CoFe_2O_4 content, and the 5% $\text{CoFe}_2\text{O}_4/\text{Ag}/\text{Ag}_3\text{VO}_4$ shows the highest degradation efficiency (the degradation rate reached 90.30% within 16 min). When the CoFe_2O_4 content is higher than 5%, the photoactivity of the $\text{CoFe}_2\text{O}_4/\text{Ag}/\text{Ag}_3\text{VO}_4$ sample decreases. The reason why the photocatalytic performance decreased may be that the surface of $\text{Ag}/\text{Ag}_3\text{VO}_4$ is covered by the excess CoFe_2O_4 , which reduces the visible light absorption by $\text{Ag}/\text{Ag}_3\text{VO}_4$. It leads to the decrease of the photocatalytic performance. As shown in Fig. 7B and C, the photocatalytic degradation kinetics of MO by using $\text{CoFe}_2\text{O}_4/\text{Ag}/\text{Ag}_3\text{VO}_4$ composites was investigated by the pseudo first-order kinetic. The photocatalytic activity of $\text{Ag}/\text{Ag}_3\text{VO}_4$ was improved with the introduction of CoFe_2O_4 . The reaction rate constants of $\text{CoFe}_2\text{O}_4/\text{Ag}/\text{Ag}_3\text{VO}_4$ composites with 0%, 1%, 5%, 10% and 20% CoFe_2O_4 are 0.04089, 0.08609, 0.13917, 0.11632 and 0.0488 min^{-1} , respectively. It can be seen that k increased with the increasing CoFe_2O_4 content to 5%. However, k decreased with further increasing CoFe_2O_4 content. Therefore, The 5% $\text{CoFe}_2\text{O}_4/\text{Ag}/\text{Ag}_3\text{VO}_4$ composites exhibit the highest degradation rate, which is about 3.4 times to that of $\text{Ag}/\text{Ag}_3\text{VO}_4$. As shown in Fig. S4, The photocatalytic activity of the mechanical mixture is obviously worse than that of 5% $\text{CoFe}_2\text{O}_4/\text{Ag}/\text{Ag}_3\text{VO}_4$. This result implies the existing interaction between CoFe_2O_4 and $\text{Ag}/\text{Ag}_3\text{VO}_4$, which is benefit for the photocatalytic activity.

The full UV–vis absorption spectra of MO during the photodegradation for 5% $\text{CoFe}_2\text{O}_4/\text{Ag}/\text{Ag}_3\text{VO}_4$ was shown in Fig. 7D. It shows

that the intensity of the absorption peak at about 463 nm weaken gradually, which means that MO was gradually photodecomposed under visible-light irradiation. The inset photograph in Fig. 7D displays that the MO dye transformed from a bright yellow to colorless. This outcome is corresponding to the results of the full UV–vis absorption spectra. In consideration of the fact that organic dyes can also harvest visible light, experiments with methyl orange photodegradation over 5% $\text{CoFe}_2\text{O}_4/\text{Ag}/\text{Ag}_3\text{VO}_4$ under different range visible-light irradiation conditions were designed to exclude the possibly evolved effects of photosensitization. From UV–vis absorption spectra [57] (see Fig. 7D and E), it can be seen that the methyl orange dyes can be excited by wavelengths of approximately 350–550 nm and hardly excited by wavelengths longer than 550~ nm, whereas the 5% $\text{CoFe}_2\text{O}_4/\text{Ag}/\text{Ag}_3\text{VO}_4$ composites can be most excited by wavelengths shorter than ~600 nm and slightly excited by a wavelength longer than 600~ nm. When the photocatalytic degradation of MO was done under visible light irradiation ($\lambda \geq 550$ nm), the methyl orange dyes cannot be excited and the 5% $\text{CoFe}_2\text{O}_4/\text{Ag}/\text{Ag}_3\text{VO}_4$ composites can be excited. The methyl orange dye can still be degraded about 50% (as shown in Fig. 7E). The effect of photosensitization during methyl orange decomposition over 5% $\text{CoFe}_2\text{O}_4/\text{Ag}/\text{Ag}_3\text{VO}_4$ is thus negligible. In other words, methyl orange decomposition can definitely be attributed to the active groups generated by 5% $\text{CoFe}_2\text{O}_4/\text{Ag}/\text{Ag}_3\text{VO}_4$.

Tetracycline (TC) has been widely used for treating bacterial infections as a broad-spectrum antibiotic agent. TC has adverse effects on each level of the hierarchical system, which is from cells to human ecosystem. Toxicity tests reveal that it can cause various adverse effects of ecosystem by inducing proliferation of bacterial drug resistance [58,59]. Therefore, it is very important to remove or decompose tetracycline. The adsorption analysis of the hybrids in the dark for the TC has been shown in Fig. S5. The adsorption–desorption balance have been also achieved between the catalyst and dye for 30 min absorption process. The photocatalytic degradation of TC in the presence of $\text{Ag}/\text{Ag}_3\text{VO}_4$ and $\text{CoFe}_2\text{O}_4/\text{Ag}/\text{Ag}_3\text{VO}_4$ hybrid materials under visible light irradiation is shown in Fig. 7F. It shows that 49.75% TC is photodegraded in the presence of $\text{Ag}/\text{Ag}_3\text{VO}_4$ after irradiated for 8 min. Among the $\text{CoFe}_2\text{O}_4/\text{Ag}/\text{Ag}_3\text{VO}_4$ hybrid materials, 5% $\text{CoFe}_2\text{O}_4/\text{Ag}/\text{Ag}_3\text{VO}_4$ composite exhibits the highest activity. It can degrade 61.48% TC (higher than that of $\text{Ag}/\text{Ag}_3\text{VO}_4$) after 8 min.

The above results confirm that 5% $\text{CoFe}_2\text{O}_4/\text{Ag}/\text{Ag}_3\text{VO}_4$ composite shows high photocatalytic activity towards colored and colorless pollutants. MO decomposition can definitely be attributed to the active groups generated by the composites, but not from the effect of photosensitization (Because MO merely excited by a wavelength longer than 550 nm). Thus, these researches show that $\text{CoFe}_2\text{O}_4/\text{Ag}/\text{Ag}_3\text{VO}_4$ composites possess excellent photocatalytic degradation performance.

3.8. Photocatalytic antibacterial activity

Fig. 8A shows the results of the antibacterial experiment of 5% $\text{CoFe}_2\text{O}_4/\text{Ag}/\text{Ag}_3\text{VO}_4$ in the dark. It can be seen that 5% $\text{CoFe}_2\text{O}_4/\text{Ag}/\text{Ag}_3\text{VO}_4$ has a clear inhibition zone of about 19.5 mm against *E. coli* (the diameter of catalysts was about 6.5 mm). This result indicates 5% $\text{CoFe}_2\text{O}_4/\text{Ag}/\text{Ag}_3\text{VO}_4$ has a good antibacterial ability in the dark. Fig. 8B shows the photocatalytic antibacterial activities of light only, $\text{Ag}/\text{Ag}_3\text{VO}_4$ and 5% $\text{CoFe}_2\text{O}_4/\text{Ag}/\text{Ag}_3\text{VO}_4$ against *E. coli* at different irradiation times. It is obvious that the amount of *E. coli* is not markedly decrease under the visible light irradiation, indicating that the *E. coli* could survive under visible light irradiation. In the presence of $\text{Ag}/\text{Ag}_3\text{VO}_4$, a small quantity of the *E. coli* was still alive after visible light irradiation for 12 min. It indicates that the $\text{Ag}/\text{Ag}_3\text{VO}_4$ has certain ability in killing the *E. coli*. In the presence of 5% $\text{CoFe}_2\text{O}_4/\text{Ag}/\text{Ag}_3\text{VO}_4$ composite, a mass

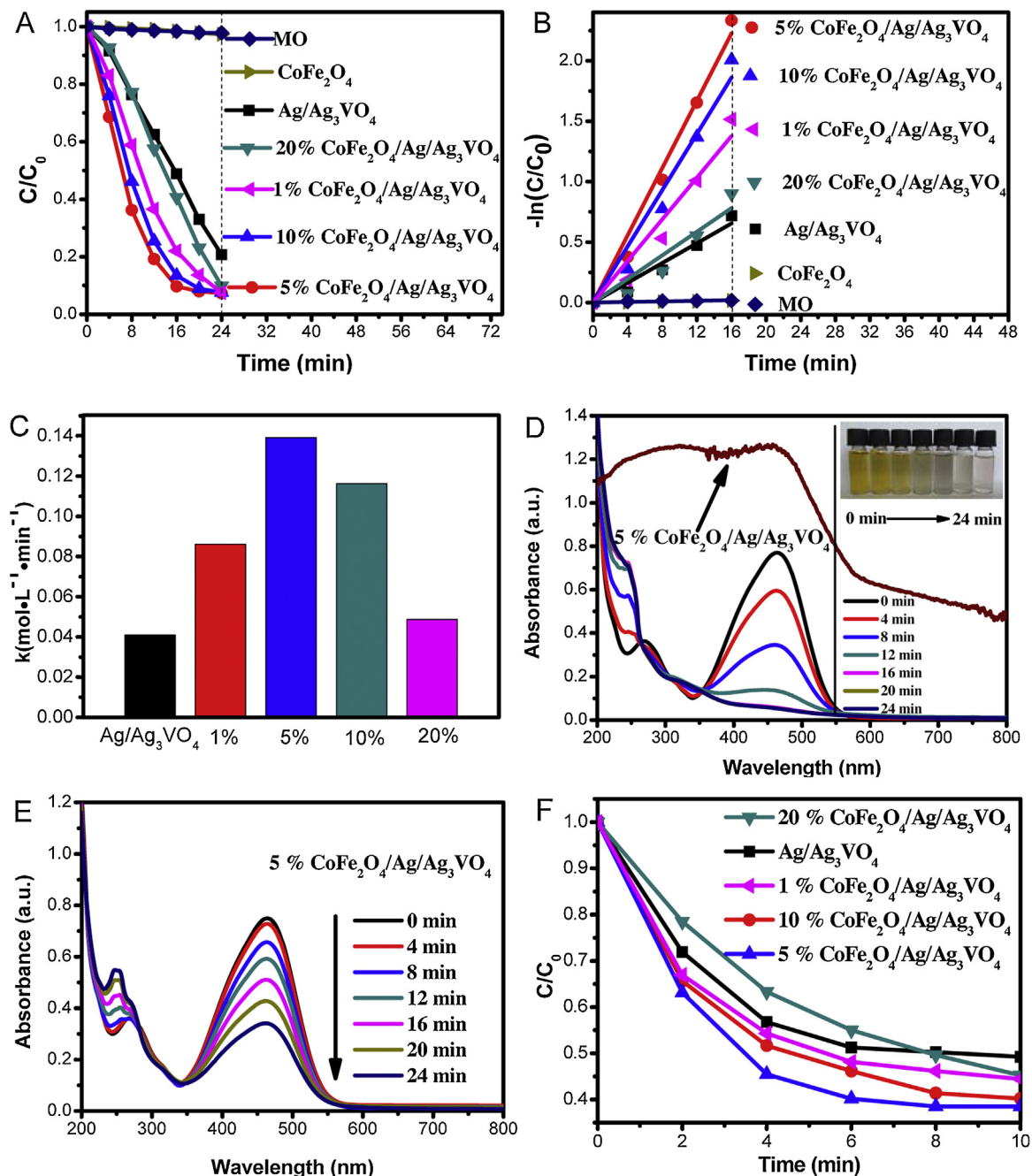


Fig. 7. (A) Photocatalytic degradation of MO with different samples under visible light irradiation; (B) Kinetic fit for the degradation of MO with (a) only light, (b) CoFe_2O_4 , (c) $\text{Ag/Ag}_3\text{VO}_4$, (d) 1% $\text{CoFe}_2\text{O}_4/\text{Ag/Ag}_3\text{VO}_4$, (e) 5% $\text{CoFe}_2\text{O}_4/\text{Ag/Ag}_3\text{VO}_4$, (f) 10% $\text{CoFe}_2\text{O}_4/\text{Ag/Ag}_3\text{VO}_4$, (g) 20% $\text{CoFe}_2\text{O}_4/\text{Ag/Ag}_3\text{VO}_4$; (C) the degradation rate constant of MO with different samples; (D) the evolution of the absorption spectra of MO over time in the presence of 5% $\text{CoFe}_2\text{O}_4/\text{Ag/Ag}_3\text{VO}_4$ (under visible light $\lambda \geq 420$ nm) and the UV-vis absorption spectrum of 5% $\text{CoFe}_2\text{O}_4/\text{Ag/Ag}_3\text{VO}_4$; (E) the evolution of the absorption spectra of MO over time in the presence of 5% $\text{CoFe}_2\text{O}_4/\text{Ag/Ag}_3\text{VO}_4$ (under visible light $\lambda \geq 550$ nm); (F) photocatalytic degradation of TC with different samples under visible light irradiation.

of *E. coli* were still alive without light irradiation. However, when the system was irradiated by visible light for 8 min, more than half of the *E. coli* was killed. When the system was irradiated for 12 min, all the *E. coli* were killed. This result reveals that 5% $\text{CoFe}_2\text{O}_4/\text{Ag/Ag}_3\text{VO}_4$ possesses antibacterial ability under visible light irradiation.

3.9. Stability of the photocatalysts

The stability of a photocatalyst is one of the most important parameters for its application. Thus, the stability of 5% $\text{CoFe}_2\text{O}_4/\text{Ag/Ag}_3\text{VO}_4$ composite was further evaluated by four

successive MO degradation experiments. In Fig. 9A, after four consecutive cycles, the photoactivity of 5% $\text{CoFe}_2\text{O}_4/\text{Ag/Ag}_3\text{VO}_4$ is still very high, which implies the stable degradation ability of $\text{CoFe}_2\text{O}_4/\text{Ag/Ag}_3\text{VO}_4$ composite. Furthermore, as shown in Fig. 9B, the XRD analysis of the 5% $\text{CoFe}_2\text{O}_4/\text{Ag/Ag}_3\text{VO}_4$ hybrid material before and after the photocatalytic reactions were carried out. It is clear that the main XRD peaks of the recycled 5% $\text{CoFe}_2\text{O}_4/\text{Ag/Ag}_3\text{VO}_4$ sample have no obvious change, which indicated that the crystal structures of the samples were not destroyed. The results show that the $\text{CoFe}_2\text{O}_4/\text{Ag/Ag}_3\text{VO}_4$ hybrid materials have the stable degradation ability and crystal structures during the photodegradation process.

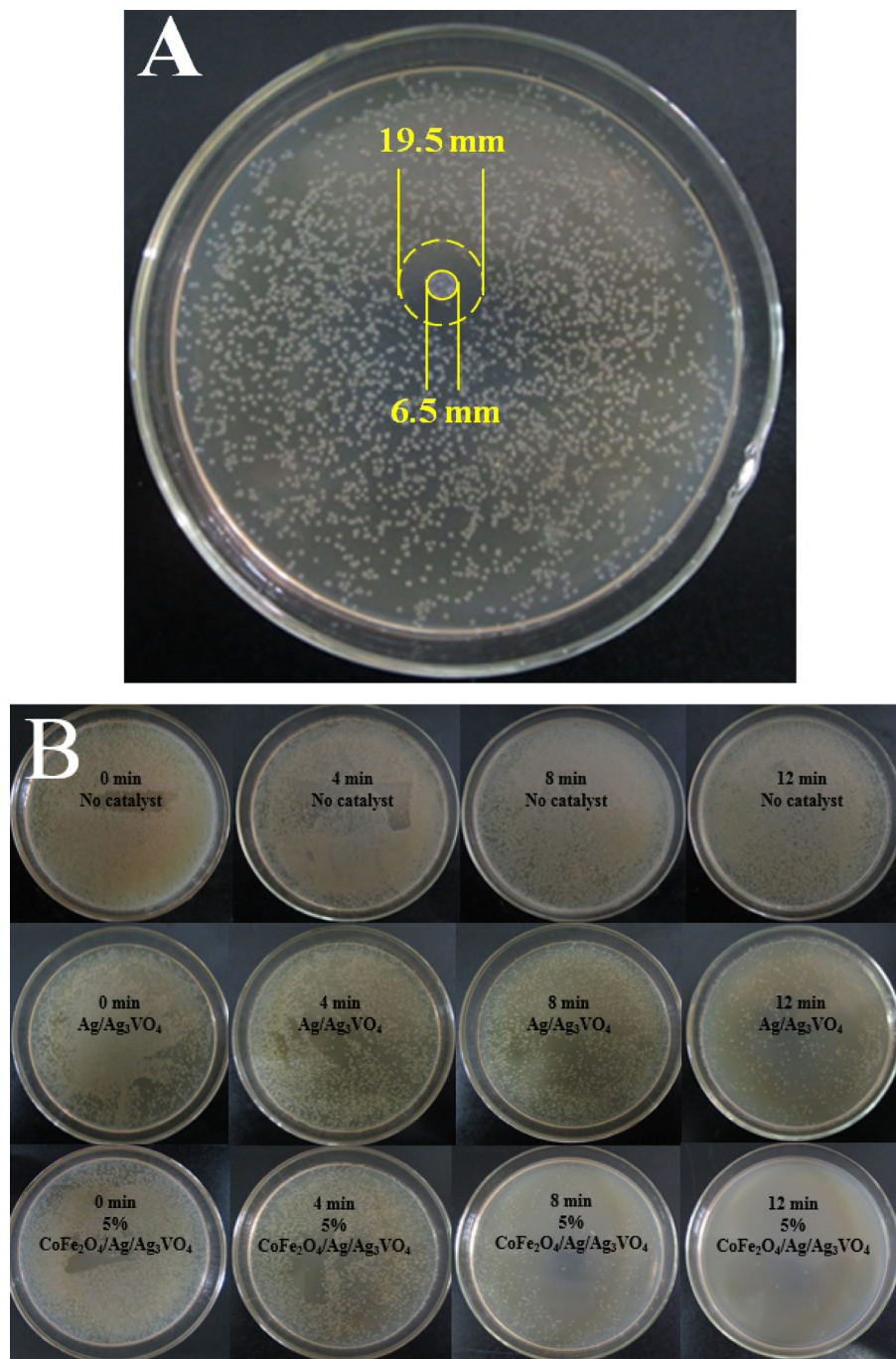


Fig. 8. (A) The representative inhibition zone of 5% CoFe₂O₄/Ag/Ag₃VO₄ disks against *E. coli* after 12 h incubation in the dark and (B) the photocatalytic antibacterial activities of light only, Ag/Ag₃VO₄ and 5% CoFe₂O₄/Ag/Ag₃VO₄ against *E. coli* at different irradiation times.

3.10. EIS and PL analysis

Electrochemical impedance spectroscopy (EIS) was carried out to investigate the migration and transfer processes of photogenerated electrons and holes in the catalyst. The radius of the arc in the EIS spectra reflects the interface layer resistance occurred on the surface of electrode. Generally, the smaller radius of the arc indicates the higher efficiency of charge transfer [60]. The Nyquist plots of Ag/Ag₃VO₄ and 5% CoFe₂O₄/Ag/Ag₃VO₄ hybrid materials before and after visible light irradiation is shown in Fig. 10. It can be seen that the arc radius of 5% CoFe₂O₄/Ag/Ag₃VO₄ hybrid materials are smaller than Ag/Ag₃VO₄, which implies a higher efficiency of charge transfer, more effective separation of photogenerated

electron-hole pairs and fast interfacial charge transfer to the electron donor/electron acceptor occurred. Furthermore, the arc radius of EIS Nyquist plot of 5% CoFe₂O₄/Ag/Ag₃VO₄ and Ag/Ag₃VO₄ under the visible light irradiation is smaller than that in the dark, suggesting the dramatically enhanced transfer and separation efficiency of photogenerated carriers and transfer rate of photoexcited electron after visible light irradiation [61–63]. All above results imply that CoFe₂O₄/Ag/Ag₃VO₄ composite has a faster interfacial charge transfer to the electron acceptor and a more effective separation of electron–hole pairs by the introduction of CoFe₂O₄, thus leading to an expected improvement in the photocatalytic activity.

Photoluminescence (PL) emission spectra are usually employed to reveal the separation and recombination efficiency of the pho-

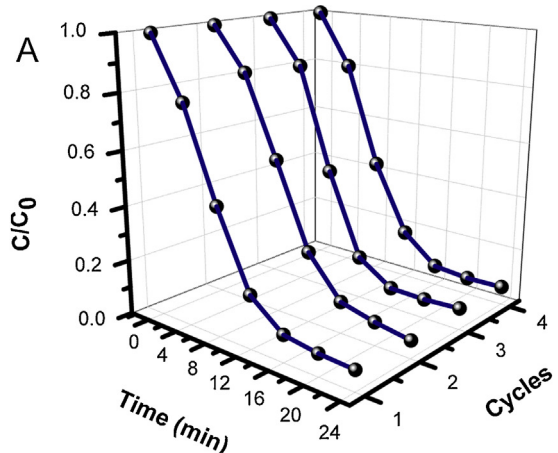


Fig. 9. (A) Four cycling runs of 5% CoFe₂O₄/Ag/Ag₃VO₄ composite for MO degradation under the visible light irradiation; (B) The XRD patterns of 5% CoFe₂O₄/Ag/Ag₃VO₄ before and after cyclic test.

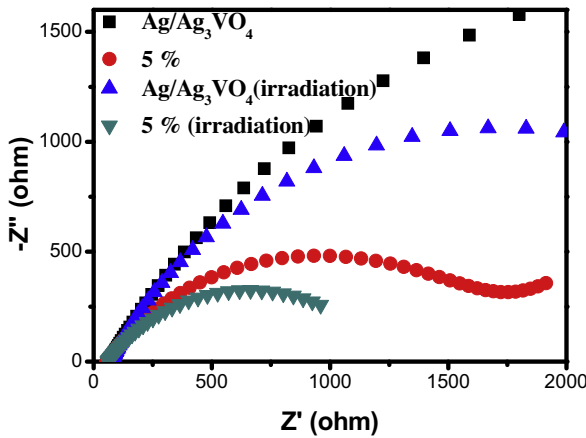


Fig. 10. Electrochemical impedance spectra of Ag/Ag₃VO₄ and 5% CoFe₂O₄/Ag/Ag₃VO₄ photocatalysts.

ogenerated electron–hole pairs in photocatalysts. The weaker emission intensity represents the lower recombination efficiency of the photogenerated carriers and the higher photocatalytic activity [58]. Fig. 11 shows the PL spectrum for Ag/Ag₃VO₄ and 5% CoFe₂O₄/Ag/Ag₃VO₄ hybrid materials. Both the samples show strong emission peak centered at around 468 nm. It can be seen that the emission intensity of the CoFe₂O₄/Ag/Ag₃VO₄ composite

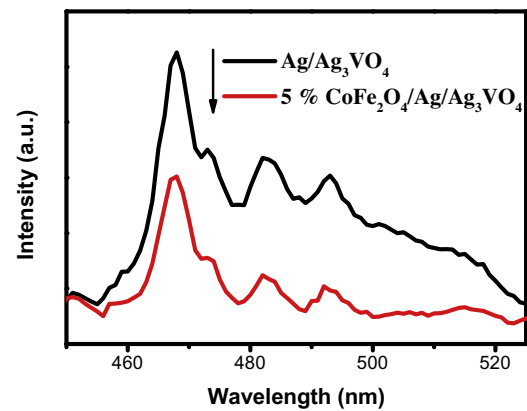


Fig. 11. PL spectra of Ag/Ag₃VO₄ and 5% CoFe₂O₄/Ag/Ag₃VO₄ hybrid materials.

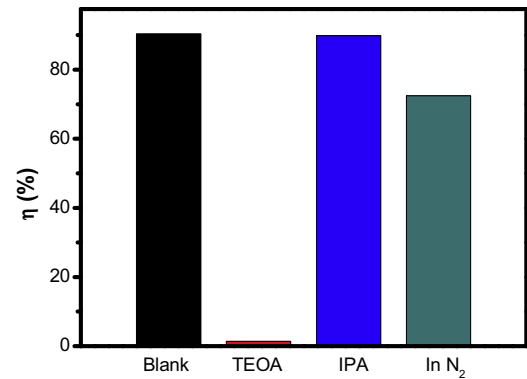


Fig. 12. Trapping experiment of active species during the photocatalytic degradation of MO over 5% CoFe₂O₄/Ag/Ag₃VO₄ sample under visible light irradiation.

is obviously weaker than that of Ag/Ag₃VO₄. This result reveals that CoFe₂O₄/Ag/Ag₃VO₄ composite has lower recombination rate of photogenerated charge carriers. The PL analysis is consistent with the EIS analysis, which further confirms that the introduction of CoFe₂O₄ is an effective way to improve photocatalytic efficiency.

3.11. Mechanism of MO photocatalytic degradation

To further distinguish the active oxygen species in the photocatalysis process over CoFe₂O₄/Ag/Ag₃VO₄ composite, free radicals trapping experiments are performed. Triethanolamine (TEOA), Nitrogen, isopropylalcohol (IPA) were introduced into the CoFe₂O₄/Ag/Ag₃VO₄ photocatalytic degradation process as scavengers for h⁺, •O₂[−] and •OH, respectively. As illustrated in Fig. 12, when iso-propanol (IPA) (1 mmol) (a scavenger for •OH) is added to the reaction system, the MO degradation is close to the reaction in the absence of radical scavengers. Therefore, the •OH is not the main active species in the reaction of the MO degradation. When the Triethanolamine (1 mmol) (quencher of h⁺) is added, it can greatly inhibit the photocatalytic degradation of MO, which implies that the h⁺ played the important role in the photocatalysis process. Furthermore, the degradation rate of MO decreased under the N₂ atmosphere (the gas flow is 200 mL/min), indicating that •O₂[−] was involved in the degradation of MO. Thus, The results indicate explicitly that the photocatalytic oxidation of MO with the CoFe₂O₄/Ag/Ag₃VO₄ catalyst mainly occurs through the synergistic effect of h⁺ and •O₂[−].

Further understanding of the photocatalytic activity of the CoFe₂O₄/Ag/Ag₃VO₄ composites was acquired by valence band XPS (denoted as VB-XPS) and UV-vis absorption spectroscopy. VB-XPS were also carried out to investigate the potentials for the top

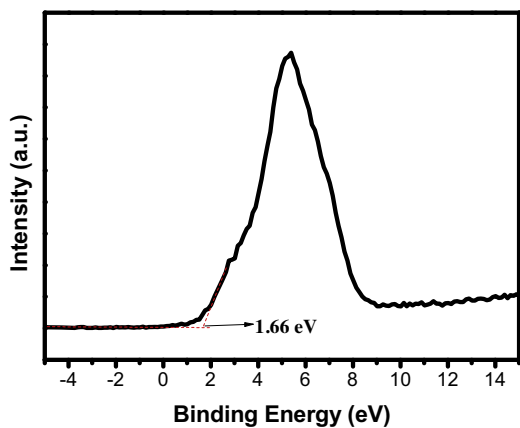


Fig. 13. Valence-band XPS spectrum of Ag/Ag₃VO₄.

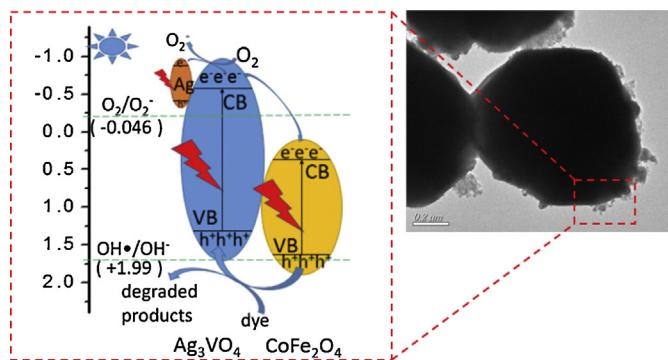


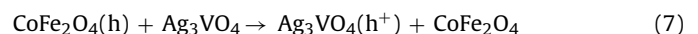
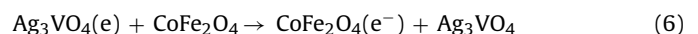
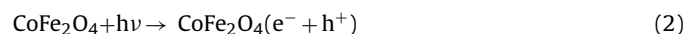
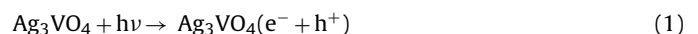
Fig. 14. Schematic diagram illustrating the degradation mechanism of organic pollutants over CoFe₂O₄/Ag/Ag₃VO₄ samples.

of the VB in the samples. Fig. 13 shows the VB-XPS spectra of Ag₃VO₄. The potential for top of VB for Ag/Ag₃VO₄ can be estimated as +1.66 eV (vs SHE), which corresponds to a previous literature [47]. According to the UV-vis absorption spectroscopy analysis, the band gap energy (E_g) of Ag/Ag₃VO₄ and CoFe₂O₄ is about 2.13 and 1.33 eV, respectively. Moreover, the conduction band (CB) edge potential of Ag/Ag₃VO₄ can be acquired by the formula E_{CB} = E_{VB} - E_g. Thus, the CB minimum will occur at about -0.47 eV. The CB and VB of CoFe₂O₄ were calculated to be +0.65 eV and +1.98 eV, respectively. Obviously, the VB potential of Ag/Ag₃VO₄ are more negative than the redox potential of OH⁻/OH (1.99 eV vs NHE) and H₂O/OH (2.7 eV vs NHE) [64], which implies that the OH⁻ and H₂O cannot be oxidized to yield OH by the h⁺ oxidation in the Ag/Ag₃VO₄, but CoFe₂O₄ is more positive than the redox potential of OH⁻/OH (1.99 eV vs NHE) and H₂O/OH (2.7 eV vs NHE), which implies that the OH⁻ and H₂O can be oxidized to yield OH by the h⁺ oxidation in the CoFe₂O₄. Similar results have also been reported that the h⁺ in the CoFe₂O₄ can oxidize the OH⁻ and H₂O to OH [36,65]. However, the results of trapping experiments indicate explicitly that the photocatalytic oxidation of MO with the CoFe₂O₄/Ag/Ag₃VO₄ catalyst mainly occurs through the synergistic effect of h⁺ and O₂⁻. Therefore, the holes in the VB of CoFe₂O₄ can not be used to degrade pollutants and will transfer to the VB of Ag₃VO₄. Meanwhile, the CB minimum of Ag/Ag₃VO₄ (-0.47 eV) is enough to reduce O₂ to generate O₂⁻ (the E₀ (O₂/O₂⁻) is only about -0.046 eV) [58,64]. The results of above mentioned and the trapping experiment are undifferentiated.

Combined with the discussion presented above and the experimental results, a possible mechanism for the degradation of MO with the CoFe₂O₄/Ag/Ag₃VO₄ photocatalyst was proposed and showed in Fig. 14. Firstly, when the CoFe₂O₄/Ag/Ag₃VO₄ photo-

catalysts are irradiated by the visible light, the electrons in the VB of Ag₃VO₄ and CoFe₂O₄ can be excited to the CB, leaving holes in the VB of Ag₃VO₄ and CoFe₂O₄, respectively. Then, localized SPR oscillations of Ag NPs generate plasmon hot electrons under visible light irradiation, which directly transfer from the Ag NPs to the CB of Ag₃VO₄. Subsequently, the photogenerated electrons transfer from Ag₃VO₄ to the CB of CoFe₂O₄. Subsequently, some electrons on the Ag nanoparticle and Ag₃VO₄ may be trapped by adsorbed O₂ in water to produce O₂⁻ radical. Holes transfer from the VB of CoFe₂O₄ to that of Ag₃VO₄. Finally, photogenerated electrons accumulate on CoFe₂O₄ and holes are collected on Ag and Ag₃VO₄, which is beneficial for interfacial charge transfer, and the photocatalytic activity is then enhanced owing to the higher separation efficiency of photogenerated carriers.

Following the information of the above results, the process for the enhancement of the photocatalytic activity of CoFe₂O₄/Ag/Ag₃VO₄ nanocomposites can be described as follows:



4. Conclusions

In summary, a new magnetic CoFe₂O₄/Ag/Ag₃VO₄ composite was prepared through a hydrothermal method. The as-prepared CoFe₂O₄/Ag/Ag₃VO₄ composite showed greatly enhanced visible-light photocatalytic activity for the degradation of colored and colorless pollutants. The experiment results show that the 5% CoFe₂O₄/Ag/Ag₃VO₄ has the highest photoactivity (the degradation rate is about 3.40 times than that of Ag/Ag₃VO₄) and magnetic ability. Furthermore, cycling experiments and the XRD patterns after cycling experiments reveal that the CoFe₂O₄/Ag/Ag₃VO₄ sample has excellent stable degradation ability and crystal structures in the photocatalytic process. The PL and EIS experiment illustrated that the synergistic effect between Ag/Ag₃VO₄ and CoFe₂O₄ promote the enhancement of the photoactivity efficiency of MO. In addition, according to the experimental results of trapping experiment, photogenerated holes are the main reactive species contributing to the excellent photocatalytic degradation of the dyes. What's more, the CoFe₂O₄/Ag/Ag₃VO₄ composite has excellent antibacterial ability. This work provides a facile way to prepare the new magnetic photocatalyst for the treatment of organic contaminants and antibacterial.

Acknowledgements

This work is financially supported by the National Natural Science Foundation of China for Youths (No. 21407065, 21506079), Natural Science Foundation of Jiangsu Province for Youths (BK20140533), China Postdoctoral Science Foundation (No.: 2014M551520, 2014M560399, 2015T80514), Jiangsu University Scientific Research Funding (No. 14JDG052).

Appendix A. Supplementary data

Supplementary data associated with this article can be found, in the online version, at <http://dx.doi.org/10.1016/j.apcatb.2016.05.049>.

References

- [1] J.G. Yu, G.P. Dai, B.B. Huang, *J. Phys. Chem. C* 113 (2009) 16394–16401.
- [2] K. Nakata, A. Fujishima, *J. Photochem. Photobiol. C: Photochem. Rev.* 13 (2012) 169–189.
- [3] X.C. Ma, Y. Dai, M. Guo, B.B. Huang, *ChemPhysChem* 9 (2012) 2304–2309.
- [4] G.P. Dai, J.G. Yu, G. Liu, *J. Phys. Chem. C* 116 (2012) 15519–15524.
- [5] H.J. Dong, G. Chen, J.X. Sun, C.M. Li, Y.G. Yu, D.H. Chen, *Appl. Catal. B* 134–135 (2013) 46–54.
- [6] S.H. Guo, J.X. Bao, T. Hu, L.B. Zhang, L. Yang, J.H. Peng, C.Y. Jiang, *Nanoscale Res. Lett.* 10 (2015) 193.
- [7] V. Sivakumar, R. Suresh, K. Giribabu, V. Narayanan, *Solid State SCI* 39 (2015) 34–39.
- [8] J. Xu, C.G. Hu, Y. Xi, B.Y. Wan, C.L. Zhang, Y. Zhang, *Solid State SCI* 14 (2012) 535–539.
- [9] S.W. Zhang, J.X. Li, X.K. Wang, Y.S. Huang, M.Y. Zeng, J.Z. Xu, *J. Mater. Chem. A* 3 (2015) 10119.
- [10] J. Wan, L. Sun, J. Fan, E.Z. Liu, X.Y. Hu, C.N. Tang, Y.C. Yin, *Appl. Surf. Sci.* 355 (2015) 615–622.
- [11] X.Y. Guo, C.F. Chen, S.Y. Yin, L.J. Huang, W.P. Qin, *J. Alloys Compd.* 619 (2015) 293–297.
- [12] Z. Hao, L.H. Ai, C.H. Zhang, Z.G. Niu, J. Jiang, *Mater. Lett.* 143 (2015) 51–54.
- [13] F. Kiantazh, A. Habibi-Yangjeh, *Mater. Sci. Semicond. Process.* 39 (2015) 671–679.
- [14] L. Zhang, Y.M. He, P. Ye, W.H. Qin, Y. Wu, T.H. Wu, *Mater. Sci. Eng. B* 178 (2013) 45–52.
- [15] D. Li, X.C. Duan, Q. Qin, H.M. Fan, W.J. Zheng, *CrystEngComm* 15 (2013) 8933–8936.
- [16] J.X. Wang, H. Ruan, W.J. Li, D.Z. Li, Y. Hu, J. Chen, Y. Shao, Y. Zheng, *J. Phys. Chem. C* 116 (2012) 13935–13943.
- [17] X.X. Hu, C. Hu, *J. Chem. Technol. Biotechnol.* 85 (2010) 1522–1527.
- [18] K. Wangkawong, S. Phanichphant, D. Tantravivat, B. Inceesungvorn, *J. Colloid Interface Sci.* 454 (2015) 210–215.
- [19] B. Inceesungvorn, T. Teeranunpong, J. Nunkaew, S. Suntalelat, D. Tantravivat, *Catal. Commun.* 54 (2014) 35–38.
- [20] L. Zhang, Y.M. He, P. Ye, Y. Wu, T.H. Wu, *Catal. Commun.* 30 (2013) 14–18.
- [21] L. Zhang, Y.M. He, P. Ye, Y. Wu, T.H. Wu, *J. Alloys Compd.* 549 (2013) 105–113.
- [22] S.M. Wang, Y. Guan, L.P. Wang, W. Zhao, H. He, J. Xiao, S.G. Yang, C. Sun, *Appl. Catal. B* 168–169 (2015) 448–457.
- [23] T.T. Zhu, Y.H. Song, H.Y. Ji, Y.G. Xu, Y.X. Song, J.X. Xia, S. Yin, Y.P. Li, H. Xu, Q. Zhang, H.M. Li, *Chem. Eng. J.* 271 (2015) 96–105.
- [24] Q. Zhu, W.S. Wang, L. Lin, G.Q. Gao, H.L. Guo, H. Du, A.W. Xu, *J. Phys. Chem. C* 117 (2013) 5894–5900.
- [25] J.C. Sun, H. Fan, B. Nan, S.Y. Ai, *Sep. Purif. Technol.* 130 (2014) 84–90.
- [26] B.Z. Tian, T.T. Wang, R.F. Dong, S.Y. Bao, F. Yang, J.L. Zhang, *Appl. Catal. B* 147 (2014) 22–28.
- [27] Y.G. Xu, T. Zhou, S.Q. Huang, M. Xie, H.P. Li, H. Xu, J.X. Xia, H.M. Li, *RSC Adv.* 5 (2015) 41475.
- [28] D.F. Zhang, X.P. Pu, K.P. Du, Y.M. Yu, J.J. Shim, P.Q. Cai, S.I. Kim, H.J. Seo, *Sep. Purif. Technol.* 137 (2014) 82–85.
- [29] X.J. Chen, Y.Z. Dai, T.H. Liu, J. Guo, X.Y. Wang, F.F. Li, *J. Mol. Catal. A: Chem.* 409 (2015) 198–206.
- [30] K.K. Senapati, C. Borgohain, P. Phukan, *Catal. Sci. Technol.* 2 (2012) 2361–2366.
- [31] Z.Y. Lu, M. He, L.L. Yang, Z.F. Ma, L. Yang, D.D. Wang, Y.S. Yan, W.D. Shi, Y. Liu, Z.F. Hua, *RSC Adv.* 5 (2015) 47820–47829.
- [32] S. Singh, N. Khare, *Mater. Lett.* 15 (2015) 64–67.
- [33] N. Wetchakun, S. Chaiwichain, K. Wetchakun, W. Kangwansupamonkon, B. Inceesungvorn, S. Phanichphant, *Mater. Lett.* 113 (2013) 76–79.
- [34] C.J. Li, J.N. Wang, B. Wang, J.R. Gong, Z. Lin, *Mater. Res. Bull.* 47 (2012) 333–337.
- [35] C. Borgohain, K.K. Senapati, K.C. Sarma, P. Phukan, *J. Mol. Catal. A: Chem.* 363–364 (2012) 495–500.
- [36] L. Gan, S.M. Shang, C.W.M. Yuen, S.X. Jiang, E.L. Hu, *Appl. Surf. Sci.* 351 (2015) 140–147.
- [37] A. Singh, D.P. Dutta, A. Ballal, A.K. Tyagi, M.H. Fulekar, *Mater. Res. Bull.* 51 (2014) 447–454.
- [38] W. Zhao, Y. Guo, S.M. Wang, H. He, C. Sun, S.G. Yang, *Appl. Catal. B* 165 (2015) 335–343.
- [39] W. Zhao, J.H. Li, Z.B. Wei, S.M. Wang, H. He, C. Sun, S.G. Yang, *Appl. Catal. B* 179 (2015) 9–20.
- [40] W. Zhao, Y. Guo, Y. Faiz, W.T. Yuan, C. Sun, S.M. Wang, Y.H. Deng, Y. Zhuang, Y. Li, X.M. Wang, H. He, S.G. Yang, *Appl. Catal. B* 163 (2015) 288–297.
- [41] S.Q. Huang, Y.G. Xu, Z.G. Chen, M. Xie, H. Xu, M.Q. He, H.M. Li, Q. Zhang, *RSC Adv.* 5 (2015) 71035.
- [42] S.Q. Huang, Y.G. Xu, M. Xie, H. Xu, M.Q. He, J.X. Xia, L.Y. Huang, H.M. Li, *Colloids Surf. A: Physicochem. Eng. Aspects* 478 (2015) 71–80.
- [43] N. Adeela, K. Maaz, U. Khan, S. Karim, A. Nisar, M. Ahmad, G. Ali, X.F. Han, J.L. Duan, J. Liu, *J. Alloys Compd.* 639 (2015) 533–540.
- [44] N. Quandt, R. Roth, F. Syrowatka, M. Steimecke, S.G. Ebbinghaus, *J. Solid State Chem.* 233 (2016) 82–89.
- [45] R. Kurchania, D. Rathore, R.K. Pandey, *J. Mater. Sci.: Mater. Electron.* 26 (2015) 9355–9365.
- [46] M. Shekofteh-Gohari, A. Habibi-Yangjeh, *Solid State Sci.* 48 (2015) 177–185.
- [47] K. Wangkawong, D. Tantravivat, S. Phanichphant, B. Inceesungvorn, *Appl. Surf. Sci.* 324 (2015) 705–709.
- [48] P. Chen, *Mater. Lett.* 163 (2016) 130–133.
- [49] X.Z. Li, Z.S. Zhang, C. Yao, X.W. Lu, X.B. Zhao, C.Y. Ni, *Appl. Surf. Sci.* 364 (2016) 589–596.
- [50] T. Aghavian, J.B. Moussy, D. Stanescu, R. Belkhou, N. Jedrecy, H. Magnan, P. Ohresser, M.A. Arrio, P. Sainctavit, *J. Electron. Spectrosc. Relat. Phenom.* 202 (2015) 16–21.
- [51] L.C. Zhou, L.Q. Ji, P.C. Ma, Y.M. Shao, H. Zhang, W.J. Gao, Y.F. Li, *J. Hazard. Mater.* 265 (2014) 104–114.
- [52] G.S. Sun, H. Xu, H.M. Li, H.M. Shu, C.T. Liu, Q. Zhang, *React. Kinet. Mech. Catal.* 99 (2010) 471–484.
- [53] H. Xu, H.M. Li, L. Xu, C.D. Wu, G.S. Sun, Y.G. Xu, J.Y. Chu, *Ind. Eng. Chem. Res.* 48 (2009) 10771–10778.
- [54] H.G. Yu, G.Q. Cao, F. Chen, X.F. Wang, J.G. Yu, M. Lei, *Appl. Catal. B* 160–161 (2014) 658–665.
- [55] G. Wang, Y. Ren, G.J. Zhou, J.P. Wang, H.F. Cheng, Z.Y. Wang, J. Zhan, B.B. Huang, M.H. Jiang, *Surf. Coat. Technol.* 228 (2013) S283–S286.
- [56] X.X. Hu, C. Hu, *J. Solid State Chem.* 180 (2007) 725–732.
- [57] Z.G. Yi, J.H. Ye, N. Kikugawa, T. Kako, S.X. Ouyang, H. Stuart-Williams, H. Yang, J.Y. Cao, W.J. Luo, Z.S. Li, Y. Liu, R.L. Withers, *Nat. Mater.* 9 (2010) 559–564.
- [58] J. Di, J.X. Xia, Y.P. Ge, H.P. Li, H.Y. Ji, H. Xu, Q. Zhang, H.M. Li, M.N. Li, *Appl. Catal. B* 168–169 (2015) 51–61.
- [59] Z.Y. Zhang, D.L. Jiang, C.S. Xing, L.L. Chen, M. Chen, M.Q. He, *Dalton Trans.* 44 (2015) 11582–11591.
- [60] T. Yan, M. Sun, H.Y. Liu, T.T. Wu, X.J. Liu, Q. Yan, W.G. Xu, B. Du, *J. Alloys Compd.* 634 (2015) 223–231.
- [61] J.Z. Li, M.J. Zhou, Z.F. Ye, H.Q. Wang, C.C. Ma, P.W. Huo, Y.S. Yan, *RSC Adv.* 5 (2015) 91177–91189.
- [62] D.M. Chen, K.W. Wang, W.Z. Hong, R.L. Zong, W.Q. Yao, Y.F. Zhu, *Appl. Catal. B* 166–167 (2015) 366–373.
- [63] X.J. Bai, L. Wang, R.L. Zong, Y.F. Zhu, *J. Phys. Chem. C* 117 (2013) 9952–9961.
- [64] B.F. Luo, D.B. Xu, D. Li, G.L. Wu, M.M. Wu, W.D. Shi, M. Chen, *ACS Appl. Mater. Interfaces* 7 (2015) 17061–17069.
- [65] Y.S. Fu, H.Q. Chen, X.Q. Sun, X. Wang, *Appl. Catal. B* 111–112 (2012) 280–287.